



Strategies for Improving Solar Energy Conversion: Nanostructured Materials and Processing Techniques

5

Monica C. So, Sung Won Yoon, and Nicole D. Mackie

Contents

5.1	Introduction	112
5.1.1	The Current Dilemma with Solar Energy Conversion	112
5.1.2	Chapter Direction and Outline	113
5.2	Enhancing Light Absorption	113
5.2.1	Perovskites and Light Harvesting	113
5.2.2	Single Organic Cation Perovskites	114
5.2.3	Mixed Organic Cation Perovskites	114
5.2.4	Metal-Organic Frameworks (MOFs) and Sensitization	115
5.2.5	Molecular Chromophores as Sensitizers	115
5.2.6	Chromophores Integrated as MOF Building Blocks	116
5.2.7	MOFs as Sensitizers	116
5.3	Enhancing Exciton Splitting	116
5.3.1	Energy Transfer Mechanisms in MOFs	116
5.3.2	Metalloporphyrins Facilitating Förster Energy Transfer	117
5.3.3	Perylene Diimides Facilitating Förster Energy Transfer	120
5.4	Enhancing Charge Separation and Collection	121
5.4.1	Importance of Processing Techniques to Improve Morphology	121
5.4.2	Liquid-Solid Interface Methods	121
5.4.3	Liquid-Liquid Interface Methods	123
5.4.4	Air-Liquid Interface Methods	127
5.5	Conclusions	131
	References	132

Author Contribution

S. Yoon and N. Mackie wrote and edited the first draft based on research and review data. M.C. So wrote, revised, and submitted the manuscript to the publishers.

M. C. So (✉) · S. W. Yoon · N. D. Mackie

Department of Chemistry and Biochemistry, California State University, Chico, Chico, CA, USA

e-mail: mso@csuchico.edu

Abstract

Organic photovoltaics, the technology to convert sunlight into electricity by employing thin films of organic semiconductors, has received increased interest due to innovations in nanomaterials and processing methods. These technological improvements have the potential to advance a new generation of low-cost, solar-powered products with small form factors. Here, we review the photophysical and chemical concepts of organic photovoltaics and discuss some recent synthesis and fabrication results as well as future challenges.

5.1 Introduction

5.1.1 The Current Dilemma with Solar Energy Conversion

To meet future demands, we must maximize our use of renewable resources while minimizing our dependence on fossil fuels. Fossil fuels collectively represent over 80% of our total energy supply, while renewable sources only account for 10%. While there are many sources of renewable energy, solar energy is one of the most abundant. In fact, the sun delivers up to 67 terawatts per year of power, which exceeds the projected global energy demand of 30 terawatts per year by 2050. Organic photovoltaics (OPVs) show promise for light-to-electrical energy conversion with the cells having power conversion efficiencies of 13.2%, but the theoretical maximum is at 32%. If efficiencies can be increased to even a fraction of the way to ca. 16%, OPVs would be more cost-competitive with their inorganic counterparts.

However, there are four major challenges in improving OPV performance. These include (a) poor light harvesting, (b) inefficient exciton splitting into holes and electrons, (c) increased recombination of separated charges at the donor/acceptor interface and (d) inefficient collection of charges at the active layer/electrode interface. The problem related to (a) results in a limited range of absorbance of visible light. The problem for (b) originates from the limited diffusion length of the exciton, typically ca. 10 nm. The problem for (c) results in the problem (d), such as partial electrical shorting. OPVs constructed from conventional materials and architectures involve conflicting design requirements, which make it difficult to address all four problems simultaneously.

The aim of this chapter is to provide an overview of nanomaterials and thin film processing techniques. Specifically, this chapter discusses nanomaterials and thin film processing techniques, which have the potential to overcome the challenges associated with conventional OPV cells. To address the problem (a), we incorporate two novel nanomaterials (perovskites and metal-organic frameworks) to expand the light collection in the near-infrared region of light. To address the problem (b), we can precisely align the chromophores in a metal-organic framework platform. To address problems (c) and (d), we can optimize optical path length and crystal-thickness by using thin film deposition techniques. These approaches can potentially lead to much higher efficiencies, based on the simultaneous resolution of the four challenges hindering OPV performance.

5.1.2 Chapter Direction and Outline

Nanomaterials and thin film processing techniques are critical to resolving the current dilemma hindering OPV efficiency. Nanomaterials consist of interchangeable components, allowing for synthetic and chemical tunability on the nanoscale. Thin film processing techniques interface nanomaterials to industrially relevant supports, which are critical for manufacturing photovoltaics.

Section 5.2 presents a chemical approach to expanding light harvesting using two new classes of materials. These classes of materials include lead-halide perovskites and metal-organic frameworks (MOFs). Lead-iodide perovskites (APbI_3 , A = monovalent cation) can be modified to improve light absorption in the near-infrared region. Since MOFs are composed of both metal cations and organic linkers, their framework can be synthetically or chemically modified to improve light harvesting in deficient regions of the solar spectrum. Both modular nanomaterials provide promise in enhancing the light collection ability of solar energy conversion schemes.

Section 5.3 provides another chemical route to enhance exciton splitting by mimicking energy transport phenomena in plants. Given that energy migration in natural photosynthesis occurs, in part, through highly ordered porphyrin-like pigments (chlorophylls), crystalline MOFs assembled from photoactive components may exhibit the same behavior. To do so, organic linkers have been used to build and modify MOFs to study long-range Förster resonance energy transfer (FRET) mechanisms. By exploiting long-range, rather than short-range, energy transport in nanostructures, the lifetime of excitons will increase.

Section 5.4 highlights several thin film processing techniques which allow for deposition of nanomaterials. These techniques must produce ultrathin, low roughness, and homogeneous coatings on industrially relevant substrates, such as silicon. We discuss solid-liquid interface methods, such as layer-by-layer deposition, a stepwise, automated liquid phase process for depositing nanomaterials into thin coatings. Liquid-liquid interface methods will also be discussed. Air-liquid interface methods are other facile approaches which produce films of subnanometer roughness. An example is the Langmuir-Blodgett method, which assembles thin films by dipping hydrophobic or hydrophilic components into a liquid subphase. These are time-efficient and cost-effective processing techniques for deposition of nanomaterials, which are important for the fabrication of solar energy conversion devices.

Section 5.5 discusses the future outlook of these materials and techniques in enhancing OPV performance.

5.2 Enhancing Light Absorption

5.2.1 Perovskites and Light Harvesting

Perovskites conform to the structure ABX_3 , in which the A and B cations are coordinated with the X anions. The cations and anions of the perovskite structure are modular. Since different monovalent cations (A^+) can be used to construct

perovskites, a range of optical properties can be obtained. This underscores the versatility of perovskites to be integrated with high performing solar cells, enabling a diversity of approaches for light-to-electricity conversion.

5.2.2 Single Organic Cation Perovskites

The most common perovskites solar cells contain methylammonium lead iodide ($\text{CH}_3\text{NH}_3\text{PbI}_3$). Though they contain methylammonium cation (MA^+ , $\text{H}_3\text{CN}^+(\text{H}_3)$), formamidinium (FA^+ , $^+\text{NH}_2 = \text{C}(\text{H})\text{-NH}_2 \dots \text{I}^-$) can replace the MA^+ . Consequently, a redshifting of the absorbance occurs, attributed to the larger size and stability of the FA^+ compared to MA^+ (Fig. 5.1) [1, 2]. This suggests that a broader spectrum of visible light can potentially be converted from light to electricity in a solar cell. The challenge with using formamidinium iodide (FA^+ precursor) is that it is more hygroscopic than methylammonium iodide (MA^+ precursor), so the former should be stored in an inert atmosphere.

5.2.3 Mixed Organic Cation Perovskites

Another modification to the perovskite structure is to include mixed cations. Pellet et al. [3] reported such an approach by studying the optical properties of mixed cation lead-based halide perovskites. Compared to unmixed cation perovskite, such as methylammonium lead iodide (CH_3NH_3) PbI_3 , the mixed-cation lead iodide perovskite (CH_3NH_3) $_{0.8}$ (HNCHNH_3) $_{0.2}$ PbI_3 exhibits a 20 nm red shift of the absorbance onset upon addition of only 20 mol % of formamidinium iodide (FAI) into the structure. As the FA^+ concentration was increased, three effects were observed: (1) the absorbance onset shifted to shorter wavelengths, (2) the absorbance of the film decreased, and (3) no change in the band gap was detected. Pellet and

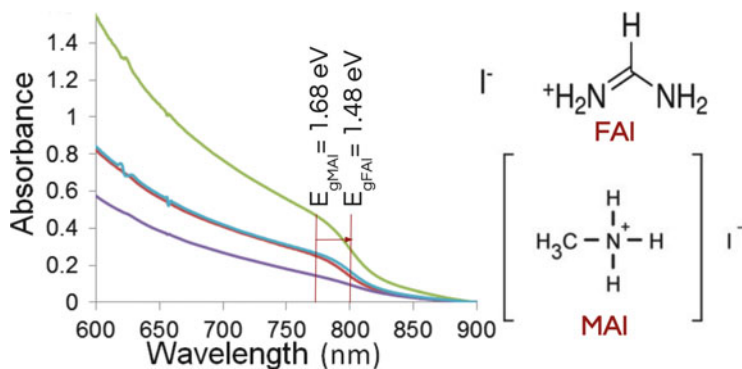
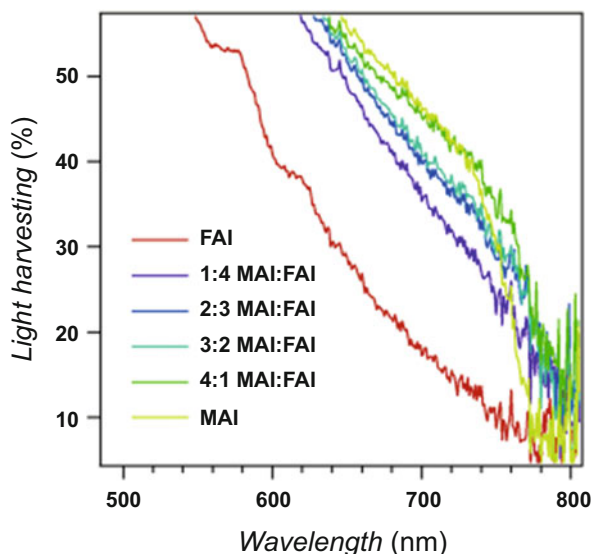


Fig. 5.1 UV-visible spectra of FAPbI_3 films are redshifted from that of MAPbI_3 , due to differences in cation structure

Fig. 5.2 Light-harvesting spectra of perovskite films show that optimized 4:1 MAI:FAI concentration redshifts the absorbance onset by 20 nm relative to the MAI sample. (Reproduced from Ref. [3] with permission from Wiley VCH)



coworkers optimized the MAI:FAI ratio of 4:1 or 3:2 (c/c) in the 2-propanol bath solution for maximizing light absorption of the perovskite into the red while maintaining the high absorption coefficient of $(\text{CH}_3\text{NH}_3)\text{PbI}_3$. Another benefit of formamidinium lead iodide is that it scatters light less strongly than methylammonium lead iodide. Therefore, the former serves as a promising organic cation to utilize in perovskite solar cells (Fig. 5.2).

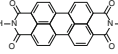
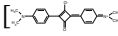
5.2.4 Metal-Organic Frameworks (MOFs) and Sensitization

Since MOFs can be assembled from a plethora of organic and inorganic building blocks, the MOFs can exhibit a diverse range of optoelectronic properties. Consequently, they can be integrated into a variety of energy conversion nanomaterials and systems [4–10].

There are examples of MOFs serving as (a) the sensitizer agent, which transfers energy to a neighboring material [11–13], and (b) the material to be sensitized. Note for the latter case, MOFs are generally synthesized with molecular chromophores (struts) to optimize exciton migration. However, the more challenging issue is to include struts that exhibit ideal absorption characteristics which overlap with the solar spectrum. Therefore, ideal MOFs for functional harvesting of solar energy must not only exhibit efficient exciton migration but also optimize solar absorption.

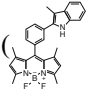
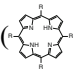
5.2.5 Molecular Chromophores as Sensitizers

To develop materials suitable for solar light absorption, MOF chemists have generally incorporated porphyrin struts [3, 14, 15]. These struts have demonstrated

directional exciton migration over several tens of struts after the initial strut has been excited. However, other than the Soret band region, porphyrins do not absorb strongly in the regions aligned with the remainder of the solar spectrum. Therefore, secondary chromophores, such as perylene diimides  and squaraine derivatives  must be installed into MOFs to account for the deficiency in solar light absorption.

5.2.6 Chromophores Integrated as MOF Building Blocks

An alternative strategy to sensitizing porphyrin MOFs is to build the MOF with an additional strut that absorbs in complementary regions of the solar spectrum. Lee and coworkers reported such an approach by building an MOF with both boron

dipyrromethene ( bodipy) and porphyrin struts ( ZnTCPP) [13]. The

bodipy absorbs in the green spectral region where the porphyrin absorbs only marginally. Additionally, this study showed that energy absorbed by the bodipy struts was efficiently (i.e., essentially quantitatively) transferred to the porphyrin struts. Thus, under green illumination, strong emission from the porphyrin was observed, even though the irradiation directly excited only bodipy. However, the longer length of the bodipy struts in the vertical direction creates a larger spacing between porphyrins in the MOF. This results in diminished lateral dipolar coupling between the porphyrins, decreasing the efficiency of exciton migration.

5.2.7 MOFs as Sensitizers

To compensate for the loss in exciton migration efficiency, an alternative approach is to mimic light-harvesting complexes in plants, such as carotenoids and reaction centers. In other words, molecules of higher exciton energy can transfer energy to those with lower exciton energy in an MOF structure [16].

5.3 Enhancing Exciton Splitting

5.3.1 Energy Transfer Mechanisms in MOFs

Since MOFs can self-assemble into ordered structures containing both donor (D) and acceptor (A) chromophores (i.e., metalloporphyrins), MOFs serve as promising platforms for monitoring the energy transport. For supramolecular systems containing weakly coupled chromophores, the Förster and Dexter energy transfer mechanisms best model the transfer of energy.

In the Förster energy transfer mechanism (Eq. 5.1) [17], the rate of intermolecular energy transfer (k_{EnT}) between a fixed pair of molecules depends on the overlap integral (OI) between the normalized emission spectrum of D and the normalized absorption spectrum of A, and the exciton coupling constant (J , cm^{-1}) between D and A (arbitrary units).

$$k_{EnT} = \frac{2\pi}{\hbar} J^2(OI) \quad (5.1)$$

The magnitude of J is related to the magnitude of the oscillator strength for excitation to the lowest singlet excited state, the fluorescence quantum yield, the separation distance (R , m) between the D and A moieties ($J^2 \propto \frac{1}{r^6}$ for point dipoles), and the angle between their transition dipoles.

Unlike Förster energy transfer which only applies to allowed transitions, the Dexter energy transfer can occur when the spin state is not conserved. Another difference is that Dexter transfer dominates over very short distances relative to those for Förster transfer. Since Dexter energy transfer depends on electronic coupling and orbital overlap of D and A, the rate of Dexter energy transfer tapers off with increased R (Eq. 5.2) [18]:

$$k_{EnT} = \frac{2\pi}{\hbar} K^2 e^{-2R/L}(OI) \quad (5.2)$$

In Eq. 5.2, L is the sum of the van der Waals radius (Å), and K is related to the degree of electronic coupling at close contact between D and A. Others have extensively observed Dexter transfer in ruthenium-based MOFs [1, 3, 5, 6, 19–29], but we highlight only MOFs exhibiting Förster energy transfer in this chapter. There are two main changes that have been demonstrated in the literature involving Förster energy transfer: (a) electronic structure of organic linkers or (b) spatial variations in the supramolecular structure.

5.3.2 Metalloporphyrins Facilitating Förster Energy Transfer

Commonly incorporated into MOFs, metalloporphyrins share structural and chromophoric features of plant chlorophylls. Since metalloporphyrin linkers are synthetically tunable, they can exhibit a wide range of light harvesting and energy transfer capabilities [30–32].

Lee and colleagues utilized a metalloporphyrin-based MOF of the pillared paddlewheel motif for one of the earliest energy transfer studies [13]. Built from dinuclear zinc clusters as nodes, bodipy as the pillar, and zinc-based tetracarboxyphenyl porphyrin (TCPP) as the paddlewheel linker, the BOP MOF emitted fluorescence upon excitation by red, blue, and green photons. Consequently, the authors observed efficient energy transfer from the antenna pillar to the primary chromophore linker (Fig. 5.3.). Despite the geometric orthogonality of its linkers,

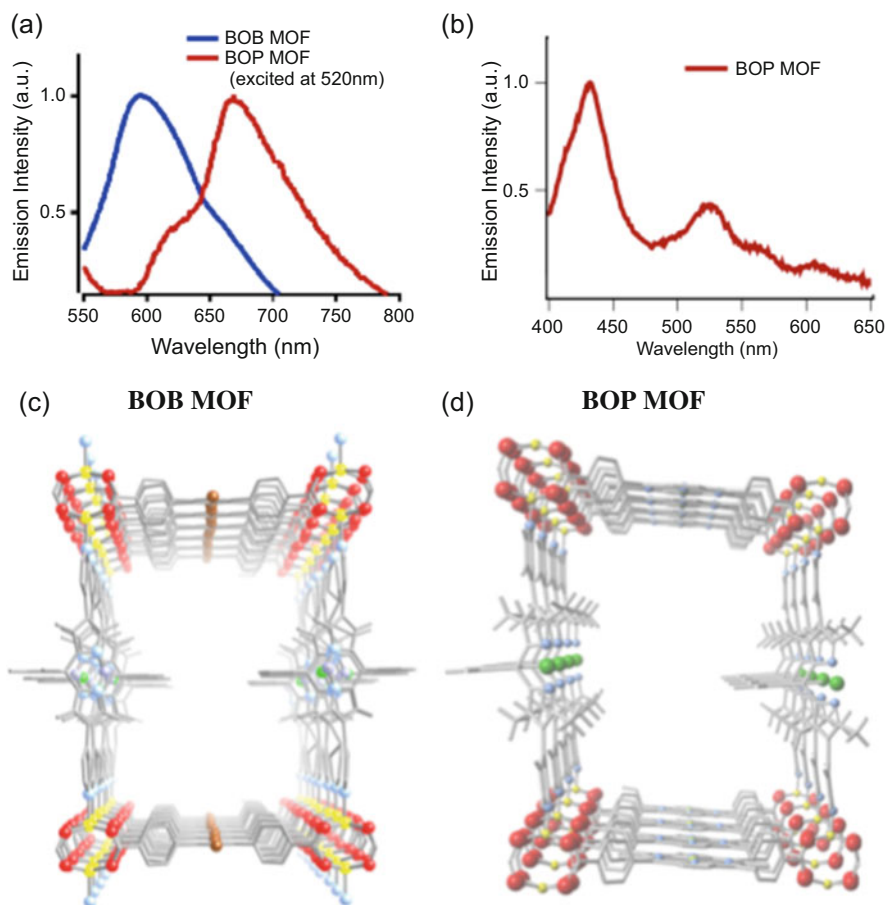


Fig. 5.3 (a) Emission spectra of BOB and BOP MOFs took at 520 nm excitation. (b) Excitation spectra of BOP and pyridine-treated BOP MOF monitored at 667 nm. Crystallographic illustration of (c) BOB MOF and (d) BOP MOF. O = red spheres, Zn = yellow spheres, C = gray segment, N = blue spheres, B = green spheres, F = white segment. (Reproduced from Ref. [33] with permission from the American Chemical Society)

energy transfer occurred due to the slight deviation of their root-mean-square value of the angle from 90° . To avoid ligand-to-metal charge transfer and resulting quenching of struts, the authors incorporated Zn(II) as metal nodes. This seminal work established that metalloporphyrin-based MOFs can be used as platforms for studying energy transfer behavior.

Given that the criteria for energy transfer directionality were vaguely defined in a metalloporphyrin-based MOF (DA-MOF), Patwardhan et al. [16] set out to investigate. He increased the anisotropy of energy transfer by replacing the TCPP linkers with a

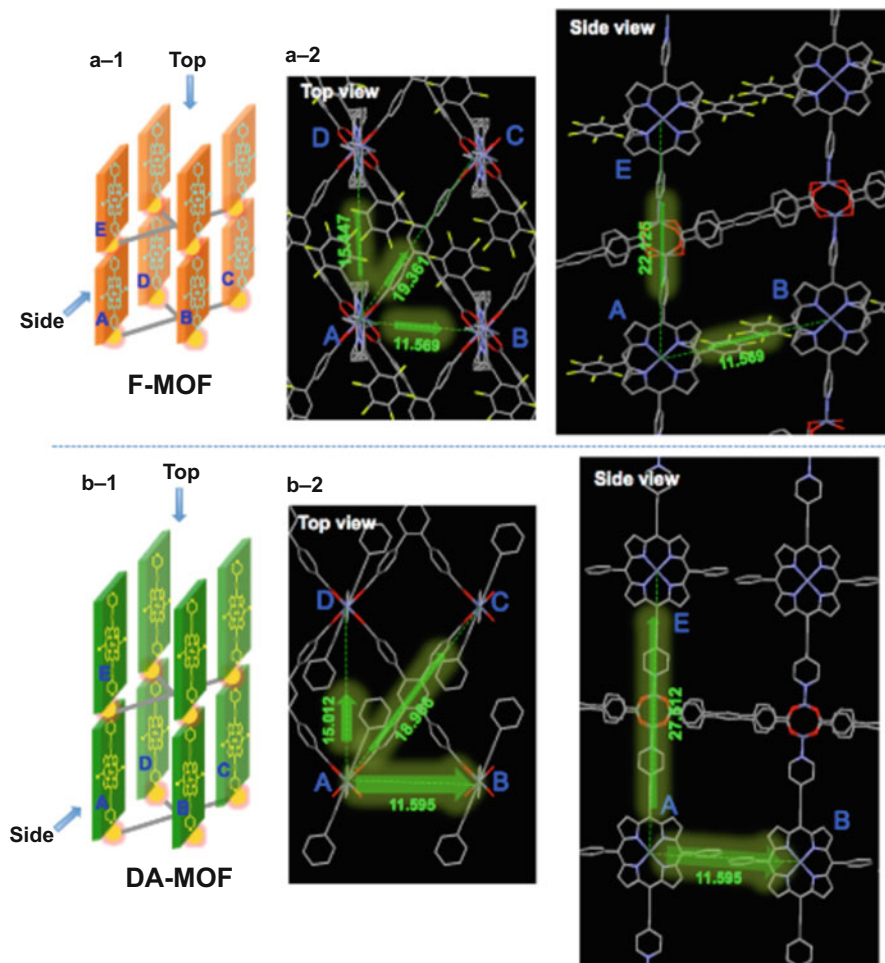


Fig. 5.4 Capped stick representations of the crystal structure of F-MOF (a-2) and DA-MOF (b-2) with arrows indicating the four energy transfer directions from A to B, C, D, and E between nearest neighboring porphyrin blocks. (Reproduced from Ref. [34] with permission from the American Chemical Society)

longer pyrene-based linker (TA-Py). This small modification increased lengths in the AB-, AC-, and AD-directions but not the AE-direction (Fig. 5.4) of the MOF. Importantly, the exciton transfer rates reduce by 60% in the AB-direction but remain the same in the AE direction when TA-Py is utilized. By spatial modifying the MOF, the anisotropy of energy transfer increased. This improves transport of excitons in planar structures, relevant for solar energy conversion devices.

5.3.3 Perylene Diimides Facilitating Förster Energy Transfer

Compounds built from perylene diimides (PDI) have been prominent acceptor components in solar energy conversion applications. This is partly attributed to their large electron affinities and high electron mobilities [35, 36]. By simply altering substituents at the perylene bay position (Fig. 5.5), the electronic and optical properties change [33, 37].

Since the linkers in MOFs are readily tunable, they can be optimized for long-range energy transfer. Having high spectral overlap between the emission of the donor and the absorption of the acceptor, the exciton can migrate efficiently from the bluest to the reddest absorber. This results in exclusive emission from the red absorbing organic linker in the MOF. By positioning chromophores within a distance that matches the exciton propagation length, complete energy transfer occurs. In other words, if the exciton needs to hop a farther distance, inefficient energy transfer occurs. Therefore, MOFs are viable candidates for investigating the nuances of long-range energy transfer.

Park, So, and colleagues [38] demonstrated that long-range energy transfer can occur in MOFs built from linkers arranged in an energy cascade manner. These structures were assembled from three chromophores: two PDI derivatives and one redder absorbing dye (S1). By synthetically modifying the PDIs, they produced chromophores with wide visible light absorption from 350 to 750 nm. Importantly, the synthetic changes of the PDIs resulted in high spectral overlap and directional energy transfer through energy cascade among the three chromophores. When the two PDIs and S1 were incorporated into thin films, the authors achieved film thicknesses on the order of the Förster radius and observed anisotropic energy transfer from a blue to a red absorber in the multicomponent MOF films. These findings are critical for not only enhancing light harvesting but exciton migration of MOF-based solar energy conversion applications.

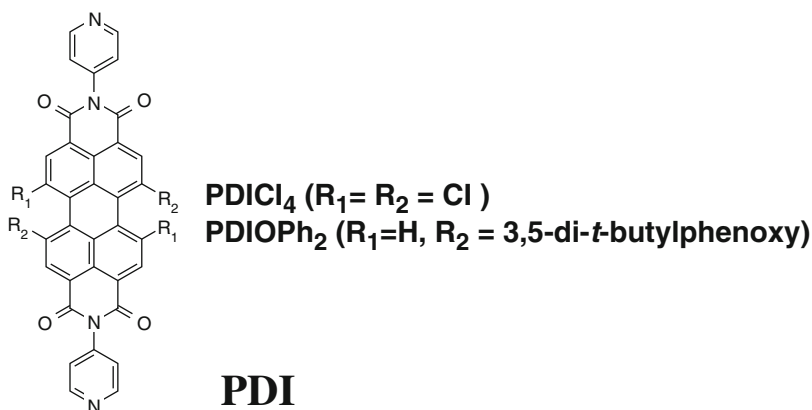


Fig. 5.5 Bay positions denoted by R in PDI molecules

5.4 Enhancing Charge Separation and Collection

5.4.1 Importance of Processing Techniques to Improve Morphology

The morphology (e.g., grain size, crystal density, uniformity, thickness) of thin film layers is intimately correlated to the charge separation and collection of energy conversion devices. Ultimately, the efficiency of the resulting solar cell device is affected. To facilitate the formation of thin film layers, one must consider suitable processing techniques. Among the most promising deposition techniques for controlling the film thickness and uniformity are liquid-solid interface methods, liquid-liquid methods, air-liquid interface methods.

5.4.2 Liquid-Solid Interface Methods

The liquid-solid interface methods hold much potential for film formation. One such method is called the layer-by-layer (LBL) method, which affords control over film thicknesses with molecular layer precision [39, 40]. Briefly, the LBL method involves a step-by-step growth method that consists of sequentially flowing solutions of the metal precursor (M^{2+}) and organic linker over a solid substrate with solvent washing steps between cycles (Fig. 5.6). During the deposition process, linkers exchange at the interface between the solid and liquid phases, allowing the metal ions to bind to linker groups at the surface and vice versa.

However, the growth mechanism of the layer-by-layer method is poorly understood. One way to elucidate its growth process is to quantify each growth step using an accurate time-resolved tool, such as a quartz crystal microbalance (QCM). In QCM, a mechanical shear oscillation can be induced by an alternating electric field. Therefore, as molecules adsorb onto the electrodes (e.g., metals, metal oxides), the oscillation frequency of the quartz crystal decreases, allowing in situ monitoring of the deposition kinetics. For rigid films, the Sauerbrey equation is often used to correlate the observed frequency shifts to deposited mass:

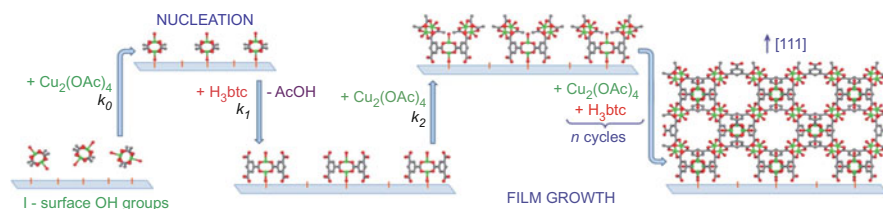


Fig. 5.6 Proposed model for stepwise growth of MOF membranes via nucleation and growth on oxide surfaces. The atoms are shown as follows: Cu = green, O = red, and C = gray. (Reproduced with permission from Ref. [39] from the Royal Society of Chemistry)

$$\Delta m = \frac{A\sqrt{\rho G}}{-2f_0^2} \Delta f$$

where Δm is the change in mass (g), A is the surface area of the resonator (cm^2), ρ and G are the density (g/cm^3) and shear modulus (Pa) of quartz, f_0 is the resonance frequency of the unloaded resonator (Hz), and Δf is the change in resonance frequency (Hz). The QCM can monitor mass changes corresponding to submonolayer film thicknesses up to several microns, so QCM can be coupled to the layer-by-layer system (Fig. 5.7) to monitor nanomaterial growth in situ [40]. Sources of error will be minimized by strict temperature control, paying careful attention to the QCM crystal surface functionalization, growing relatively thin coatings of rigid films, and optimizing the flow rates used during deposition to minimize instrument noise.

To fully harness the potential of the layer-by-layer method, the reaction conditions for each MOF film need to be carefully selected. Automating the layer-by-layer method enables scientists to test a variety of concentrations of metal and linker solutions and reaction timing of each deposition step. Further, a range of different pre-treatments of the substrate (e.g., self-assembled monolayers, pre-soaking in precursor solution) can be tested to determine optimal growth of MOF film. To process MOFs into films, conditions cannot be generalized and must be determined on a case-by-case basis.

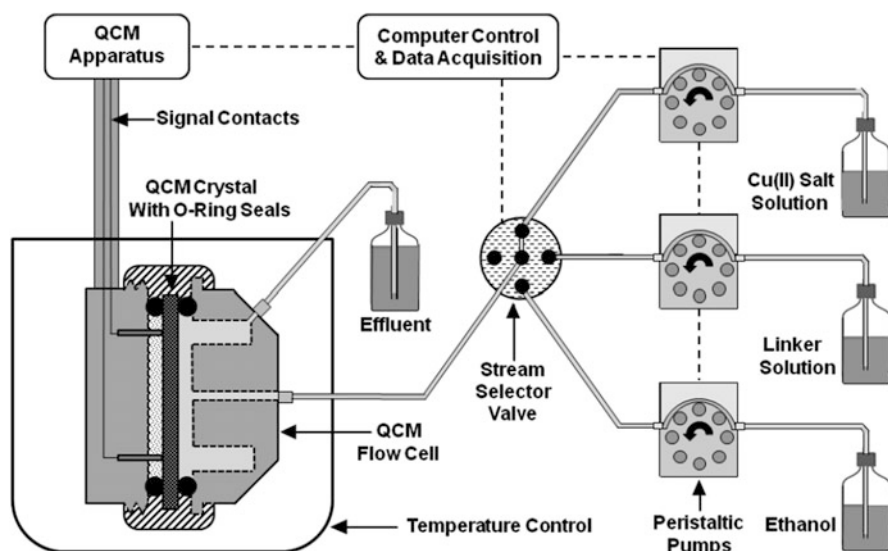


Fig. 5.7 Schematic diagram for QCM setup interfaced with layer-by-layer (LBL) deposition system. Computers control the motion of peristaltic pumps, which controls the introduction of each metal and linker precursor in a step-by-step process to form the thin membranes in a flow cell. Rinsing steps separate each deposition step to remove unreacted precursors from the flow cell, located inside the temperature-controlled QCM. (Reproduced from Ref. [39] with permission from the Royal Society of Chemistry)

5.4.3 Liquid-Liquid Interface Methods

Liquid-liquid interface method is another way to fabricate a film between two interfaces. Langmuir-Blodgett (LB) technique is one example of a liquid-liquid interface method. Sathaye and colleagues applied the LB technique to fabricate cadmium sulfide film using a 10^{-5} M cadmium carbonate solution in double-distilled water, an aqueous subphase, and a 10^{-6} M solution of carbon disulfide (or other sources of sulfide ion) in carbon tetrachloride to form a thin membrane interface (Fig. 5.8) [41]. Though LB technique and other liquid-liquid interface methods appear to be straightforward, there are a few criteria that need to be considered, such as changes in the concentration of reagents, reaction temperature and time. Several studies have found that these factors can contribute to the type of products, particle size, thickness, and film coverage.

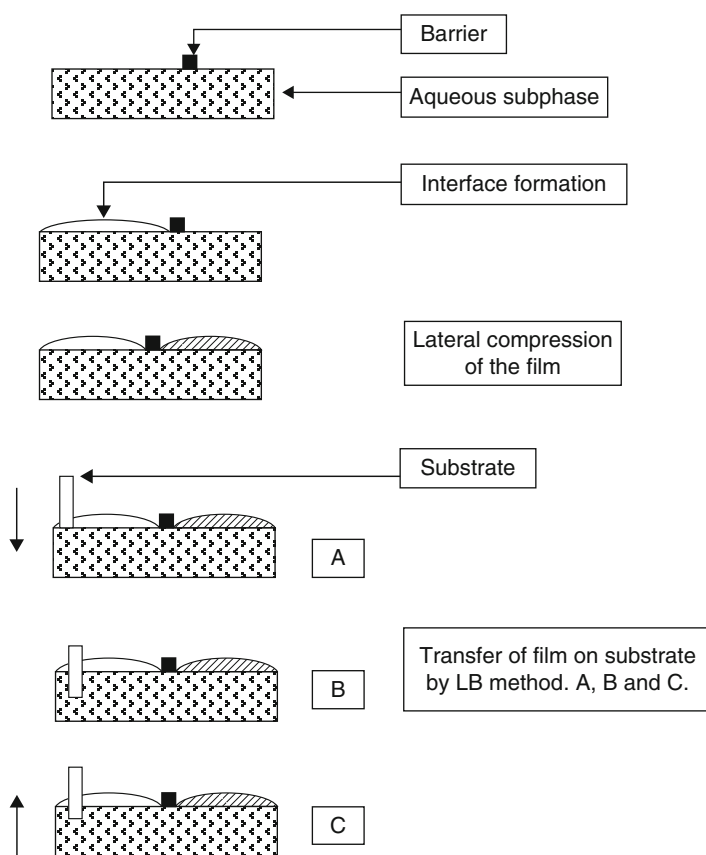


Fig. 5.8 Schematic of the LB technique. (Reproduced from Ref. [42] with permission from the American Chemical Society)

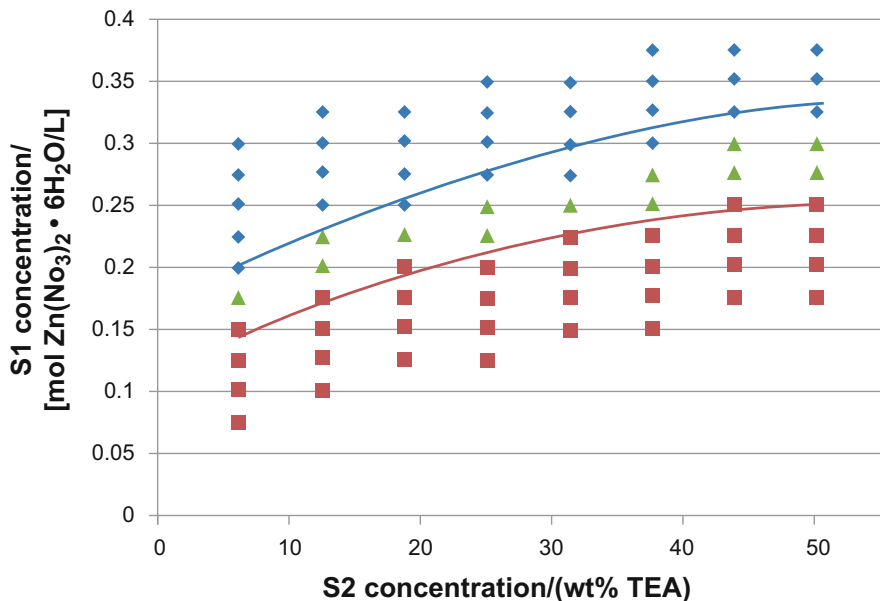


Fig. 5.9 Three different types of formation of the product depending on the concentration of two liquids; only membrane formation (diamonds), only particles formation (squares), both membrane and particles (triangles). (Reproduced from Ref. [41] with permission from the American Chemical Society)

The effect of concentrations on the form of the product can be seen in the research from Zhu and colleagues. They investigated 16 different precursor concentrations ranging from 0.025 to 0.4 mol/L with 0.025 mol/L increment and 8 different catalyst solution concentrations ranging from 6.25 to 50 wt% triethylamine (TEA, $C_6H_{15}N$) in hexane (C_6H_{14}) with 6.25% increment. Figure 5.9 shows three different shapes, diamond, triangle, and square, which represent the types of the products [41]. The concentration of metal precursor and the reducing agent is also found in the research conducted by Rao and colleagues. As the concentration of the metal precursor increased, they observed the increase in the number of the particles in nanocrystalline films as well as the thickness of the films [44]. On the other hand, when the concentration of the reducing agent was increased, less uniform films were fabricated (Fig. 5.10). The metal precursor and reducing agent are chloro(tri-phenylphosphine)gold(I) $[Au(PPh_3)Cl]$ in toluene (C_7H_8) and tetrakis-hydroxymethyl phosphonium chloride (THPC, $[P(CH_2OH)_4]Cl$) in sodium hydroxide (NaOH), respectively. The transmission electron micrographs (TEM) in Fig. 5.11 show more uniform films since they had lower concentrations of reducing agent [45].

Reaction temperatures are another significant factor for film morphology. Figure 5.11 shows TEM of nanocrystalline Au films fabricated at four different reaction temperatures. The increase in temperature results in the increase of the mean

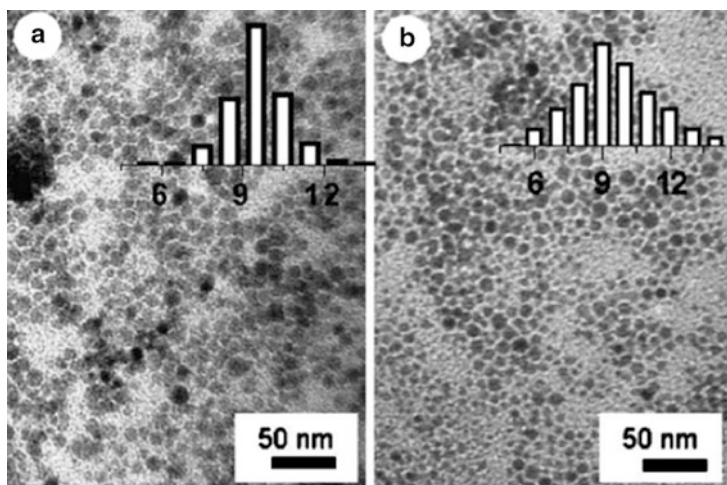


Fig. 5.10 TEM images of Au films when the concentration of reducing agent, THPC, was increased from 330 μL to (a) 660 and (b) 1200 μL . Bar graphs indicate the particle size distribution. (Reproduced from Ref. [43] with permission from the American Chemical Society)

diameters of the nanocrystals while the interparticle separation is nearly consistent. In addition, X-ray diffraction (XRD) patterns showed the growth of (111) peak, which suggests the increase in the particle size (Fig. 5.12) [44]. The effect of changing the temperature on film morphology was observed through scanning electron micrographs (SEM) as well. As Fig. 5.13 shows, the films fabricated at 30 $^{\circ}\text{C}$ had more holes and cracks, compared to those fabricated at 60 $^{\circ}\text{C}$ [45].

Reaction times can also contribute to the morphology of films. Rao and colleagues observed the increase in the film coverage with longer reaction time. Figure 5.14 shows that films made after 3, 6, and 9 h of contact time can be compared to films in Fig. 5.11, which reacted for 24 h [45]. In fact, a reaction time also contributes to the change in the diameter and thickness of the [cadmium sulfide] CdS films. Stansfield and colleagues found that the reaction time played an important role in diameter. The trend showed the growth of a diameter with the increase in the time. It showed a significant change with reaction time up to 5.2 h and a slight change up to 15 h. After 15 h, there were no changes observed [46]. The effect of reaction time on a thickness of the films is shown in Fig. 5.15b. The trend showed that a thickness of the films grew with an increase of the reaction time. It showed an even sharper change in the range from 4.5 to 5.0 h [46].

Varying these factors result in different configurations of nanocrystalline films. Changes in concentration can form three types of products: only membrane, only particles, and both membrane and particles. It also influenced the thickness of the films. In addition, changes in reaction temperature can differ the particle size of the film. Changes in reaction time made a difference in the film coverage, diameter, and thickness of the films.

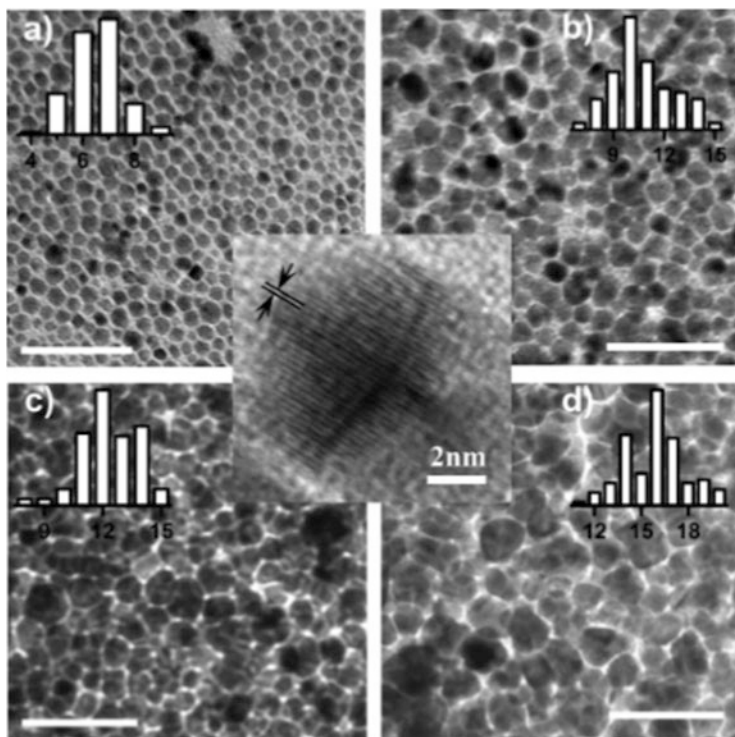
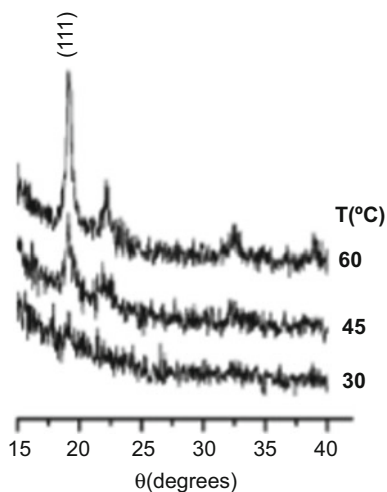


Fig. 5.11 TEM of nanocrystalline Au films with four different reaction temperatures: (a) 30, (b) 45, (c) 60, and (d) 75 °C. Bar graphs indicate the particle size distribution. The scale bars are 50 nm. The image in the middle shows an individual particle. (Reproduced from Ref. [43] with permission from the American Chemical Society)

Fig. 5.12 XRD patterns of nanocrystalline Au films with different reaction temperatures. (Reproduced from Ref. [44] with permission from the American Chemical Society)



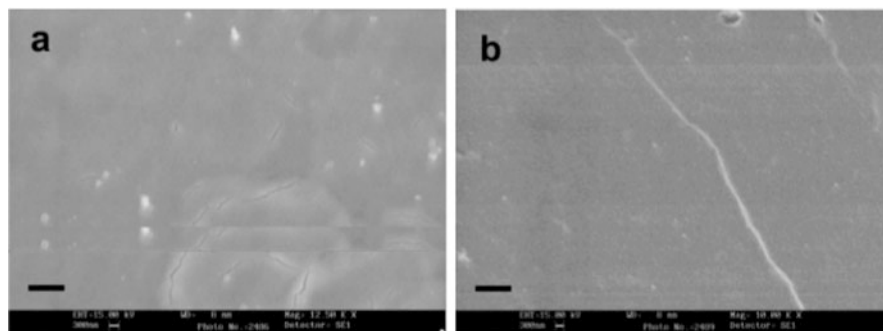


Fig. 5.13 SEM images of nanocrystalline Au films at two different temperature: (a) 30 and (b) 60 °C. (Reproduced from Ref. [45] with permission from the American Chemical Society)

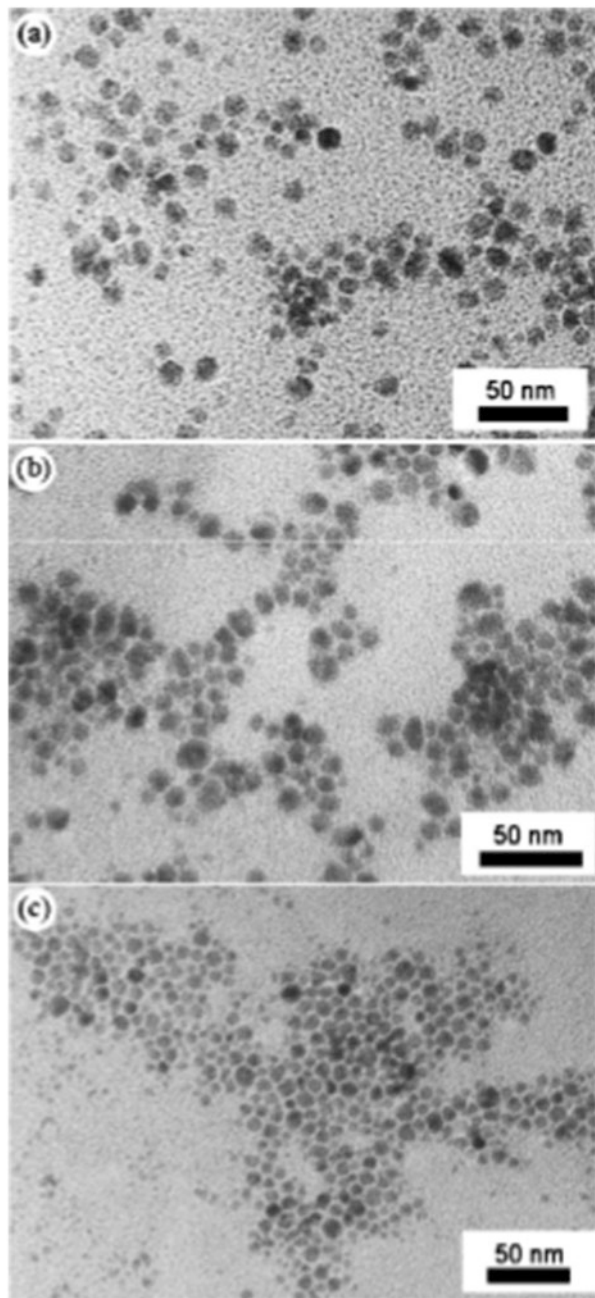
5.4.4 Air-Liquid Interface Methods

For materials to be utilized in energy conversions devices, they must be processed into thin films. Ideally, these materials should share structural and electrical similarities to that of graphene. Several MOFs have been synthesized and exhibit desirable graphene-like properties. One MOF in particular, $\text{Ni}_3(2,3,6,7,10,11\text{-hexa-iminotriphenylenesemiquinonate})_2$ or $\text{Ni}_3(\text{HITP})_2$ (Fig. 5.16a), is an attractive candidate, due to its fully conjugated pi-system. This results in a high conductivity and low thermal conductivity, which are attractive for use in electronic devices. Sheberla and colleagues synthesized identified $\text{Ni}_3(\text{HITP})_2$ as one of the most conductive MOFs. In fact, its film yields 40 S/cm – the highest conductivities achieved for this class of materials (Fig. 5.16b) [47].

Although Sheberla and colleagues were successful in depositing a film, the material was far too rough and thick for more efficient solar cell applications. Wu et al. successfully deposited $\text{Ni}_3(\text{HITP})_2$ MOF into a film, via growth at an air-liquid interface (Fig. 5.17). The procedure entails mixing the metal and organic reactants together in a beaker until thin films form at the air-liquid interface. At that point, a stamp with a substrate lifts the membrane from the interface. The MOF membrane was composed of thin and ultra-smooth nanolayers, as observed by the scanning electron microscopy (SEM) images in Fig. 5.18. This procedure allowed the MOF to be incorporated and tested as a field effect transistor (FET). Like the sample prepared by Sheberla, the film had a conductivity of 40 S/cm at room temperature [50].

However, the deposition of the film using these stamping techniques is not straightforward and complicated by experimental conditions. These include the base used to deprotonate the linker, the concentration of species, and the timing to start and end stamping [51]. For instance, Wu and his colleagues used the base in excess to catalyze the reaction. The base deprotonates the nitrogen and makes it more nucleophilic for the reaction with the Ni^{2+} cation. In unpublished work, So and colleagues studied the effects of replacing the original base (ethylamine, $\text{C}_2\text{H}_7\text{N}$) with butylamine ($\text{C}_4\text{H}_{11}\text{N}$) and octylamine ($\text{C}_8\text{H}_{19}\text{N}$). Just like ethylamine,

Fig. 5.14 TEM images of Au films with different reaction time; (a) 3, (b) 6, and (c) 9 h. (Reproduced from Ref. [45] with permission from the American Chemical Society)



butylamine was able to form the $\text{Ni}_3(\text{HITP})_2$ MOF films at 60°C , but octylamine had a very little reaction with the linker. The pK_a values of triethyl- $[-(\text{CH}_2\text{CH}_3)_3]$, tributyl- $[\text{CH}_3(\text{CH}_2)_3\text{O}]_3$, and triethylamine $[\text{C}_6\text{H}_{15}\text{N}]$ are 10.78, 10.89, and 10.08, respectively. Although it is not substantial, octylamine is less nucleophilic than the

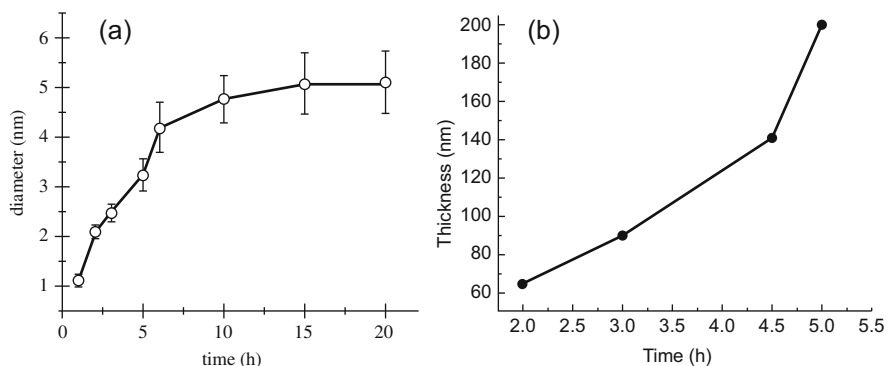


Fig. 5.15 The influence of reaction time in (a) diameter and (b) thickness of particles in CdS films. (Reproduced from Ref. [46] with permission from the American Chemical Society)

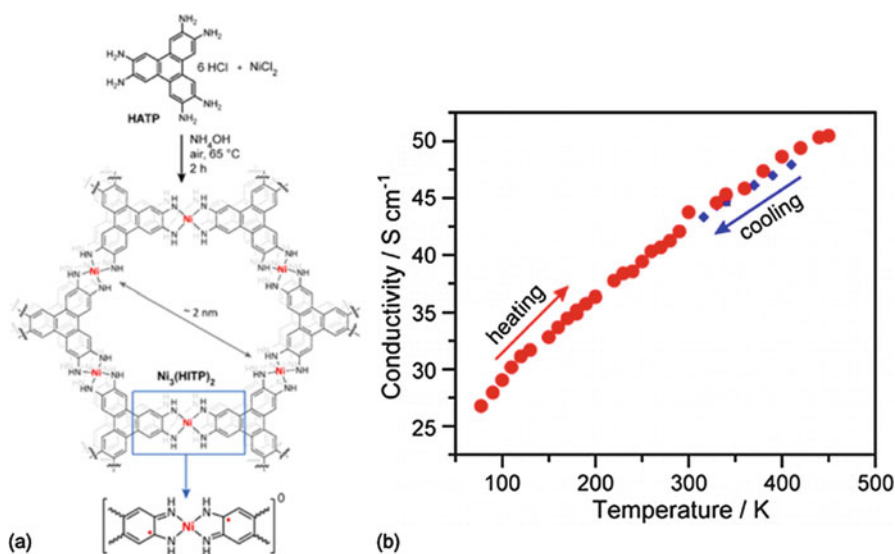


Fig. 5.16 (a) The conjugated structure of the Ni₃(HITP)₂ endows the MOF material with high conductivities. (b) Resulting MOF shows that conductivity increases with temperature. (Reproduced from Ref. [47] with permission from the American Chemical Society)

other two amines and far more sterically hindered. This makes the lone pair of electrons less readily available to react as compared to the other two amines.

The concentration of the reactants – nickel cation and organic linker – must also be sufficient to react with one another to form the desired MOF. If concentrations are too low, the reactants do not react in a timely manner to form a film at the surface. At higher concentrations, a thicker, more viscous film forms at the air-liquid interface. In a work by Rao, increasing the concentration of the gold metal increased the number of crystals and film thickness of the film [45]. This concentration is key for the synthesis of Ni₃(HITP)₂ films, since controlling the concentration to favor the

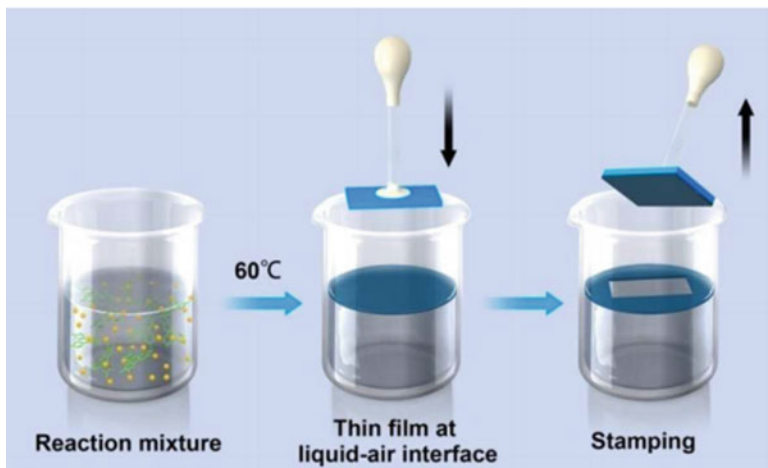


Fig. 5.17 Stamping method for film formation on a silicon substrate. (Reproduced from Ref. [49] with permission from the American Chemical Society)

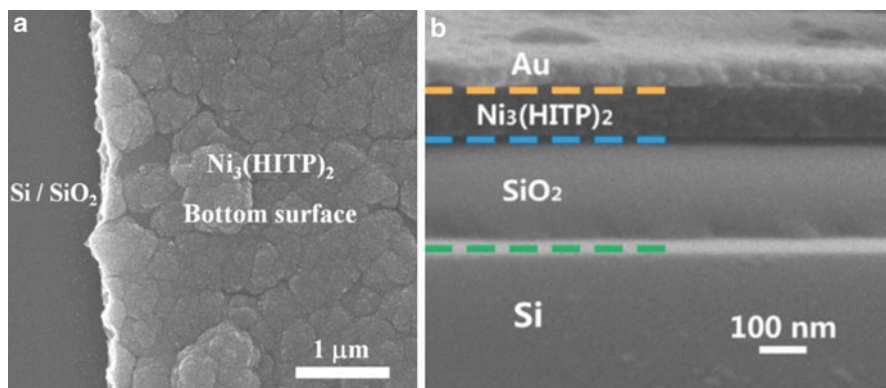


Fig. 5.18 SEM images of (a) bottom-surface of freestanding $\text{Ni}_3(\text{HITP})_2$ membrane, showing highly uniform surface and the (b) cross section of $\text{Ni}_3(\text{HITP})_2$ -based FET. (Reproduced from Ref. [49] with permission from the American Chemical Society)

formation of ultrathin films is essential for the transistor to function without causing device problems, such as short-circuiting. Another paper by Lu et al. found consistent results during the synthesis of zinc-based films via a liquid-liquid interface. When the reactants are in relatively low concentrations during the reaction, the material does not form a film and instead sinks to the bottom of the reaction vessel. At high concentrations, the resulting film is thicker and more viscous, which, as seen in work by Wu, is not ideal for an ultrathin film for FET applications [49]. The conditions necessary for liquid-liquid interface methods should be similar to that of

the air-liquid interface methods. The concentration must be optimized and be able to form a film within a reasonable amount of time that exhibits the desired thickness.

The temperature must also be regulated for proper film growth and suitable reaction time. The temperature must be high enough to quickly form the MOF. If the reaction proceeds too quickly, however, the film is disrupted by the formation of clumps before the stamping can occur. Therefore, an ultra smooth film will not be deposited on the substrate. The temperature must also be low enough to allow time for stamping and ideal film deposition onto the substrate. In contrast, if the temperature is too low, the MOF is unable to form a sufficient film at the air-liquid interface and is less likely to physisorbed to the surface of the substrate. Rao and colleagues demonstrated that the liquid-liquid interface growth of Au film depends on the temperature during synthesis. In fact, the temperature influences the diameter of the nanocrystals. Furthermore, temperatures of 30, 45, 60, and 75 °C formed nanocrystals with diameters of 7, 10, 12, and 15 nm, respectively [45]. When applied to the $\text{Ni}_3(\text{HITP})_2$ material, it is important to control the crystal size to ensure that the films possess a smooth and uniform surface. This limits grain boundaries, which optimizes conductivity.

To improve reproducibility of films, automating the process will minimize the multiple sources of error. Wu et al. observed that the thickness of the film can be determined by reaction time, but human error in timing may cause irreproducibility under the same reaction conditions [49]. Automation of the process, such as in the layer-by-layer synthesis method, can improve such efforts. The optimization of $\text{Ni}_3(\text{HITP})_2$ MOF synthesis via air-liquid interfacial film growth can be transferrable to other MOFs. Ultimately, we can construct a more generalized synthetic procedure and allow for more direct comparisons among other MOF film candidates.

5.5 Conclusions

Enhancing the performance of photovoltaics by incorporating novel materials and processing techniques presents different sets of challenges. Perovskites and MOFs have drawbacks that must be overcome before incorporating them into conversion schemes. Solid-liquid, liquid-liquid, and air-liquid interface methods still need to be optimized to make ultrathin, homogeneous, and low roughness coatings.

To resolve issues involving the first step (light harvesting), we can improve the absorption features of perovskites and MOFs to better align with that of the solar spectrum. For perovskites, varying single and mixed cations and their ratios can dramatically redshift their absorption features into the near-infrared region. For MOFs, modifying chromophoric linkers to absorb more of visible light and near-infrared regions will be critical. Alternatively, this can be done by sensitizing MOFs with secondary chromophores or quantum dots. However, a monolayer or less of sensitizer materials on the planar surface of an MOF does not have enough extinction to produce a significant increase in solar absorption efficiency. To overcome this issue, we can embed additional chromophores into the pores of MOFs without

impacting electronic coupling between the struts that support exciton flow. For either perovskites or MOFs, if the thickness of the materials exceeds the exciton transport length, some excitons will not be captured and the quantum efficiency of the perovskites or MOF in a solar cell device will suffer.

To resolve the challenges of the second step (exciton separation), we need to optimize the parameters of the Förster energy transfer rate. This includes but is not limited to chromophore and framework symmetry, fluorescence quantum yield, chromophore oscillator strength, and others. Since exciton transport is diffusive, we would require the construction of chromophore cascades to improve directionality of exciton transport. This must all be done without compensating for the structural integrity and increasing defect site density within MOFs.

To resolve problems related to the third (charge transport) and fourth (charge collection) steps, we need to improve film processing techniques. Ideally, once an exciton has reached its intended destination, they should participate in interfacial electron or hole transfer to a proximal electrode. However, holes or electrons often recombine, reducing charge collection efficiency, due to the presence of defects in the bulk film. Additional investigations are required to elucidate crystal growth dependence on temperature, annealing times, and annealing temperatures [51]. For MOF materials to be sandwiched between electrodes, the MOF orientation must be optimized to facilitate the anisotropic flow of energy and charges to the electrodes. Further, interfacial charge transfer will need to be understood and optimized. The ties between the diversity of fabrication approaches and resulting film morphology and optoelectronic and performance properties must be simultaneously understood and optimized before we can make advancements.

Acknowledgments We acknowledge the release time for M.C.S from Office of Research and Sponsored Programs at California State University, Chico (CSUC), and CSU Council on Ocean Affairs, Science & Technology. We also thank the faculty members from the Faculty Learning Communities of Office of Faculty Development at CSUC for their helpful comments and suggestions on this book chapter.

References

1. N. Ahn, S.M. Kang, J.W. Lee, M. Choi, N.G. Park, Thermodynamic regulation of $\text{CH}_3\text{NH}_3\text{PbI}_3$ crystal growth and its effect on the photovoltaic performance of perovskite solar cells. *J. Mater. Chem. A* **3**, 19901–19906 (2015)
2. J.L. Barnett, V.L. Cherette, C.J. Hutcherson, M.C. So, Effects of solution-based fabrication conditions on morphology of lead halide perovskite thin film solar cells. *Adv. Mater. Sci. Eng.* (2016). <https://doi.org/10.1155/2016/4126163>
3. N.P. Pellet, P. Gao, P. Gregori, T.Y. Yang, M.K. Nazeeruddin, J. Maier, M. Grätzel, Mixed-organic-cation perovskite photovoltaics for enhanced solar-light harvesting. *Angew. Chem. Int. Ed.* **53**(12), 3151–3157 (2014)
4. S. Jin, H.J. Son, O.K. Farha, G.P. Wiederrecht, Energy transfer from quantum dots to metal-organic frameworks for enhanced light harvesting. *J. Am. Chem. Soc.* **135**(3), 955–958 (2013)
5. G. Lu, S. Li, Z. Guo, et al., Imparting functionality to a metal-organic framework material by controlled nanoparticle encapsulation. *Nat. Chem.* **4**, 310 (2010)

6. J. Lin, X. Hu, P. Zhang, et al., Triplet excitation energy dynamics in metal-organic frameworks. *J. Phys. Chem. C* **117**, 22250 (2013)
7. C.A. Kent, D. Liu, A. Ito, et al., Rapid energy transfer in non-porous metal-organic frameworks with caged Ru(bpy)₃²⁺ chromophores: Oxygen trapping and luminescence quenching. *J. Mater. Chem. A* **1**, 14982–14989 (2013)
8. W.A. Maza, S.R. Ahrenholtz, C.C. Epley, C.S. Day, A.J. Morris, Solvothermal growth and photophysical characterization of a ruthenium(II) tris-(2,2'-bipyridine)-doped zirconium UiO-67 metal-organic framework thin film. *J. Phys. Chem. C* **118**, 14200–14210 (2014)
9. W.A. Maza, A.J. Morris, Photophysical characterization of a ruthenium(II) tris-(2,2'-bipyridine)-doped zirconium UiO-67 metal-organic framework. *J. Phys. Chem. C* **118**, 8803–8817 (2014)
10. D.E. Williams, J.A. Rietman, J.M. Maier, et al., Energy transfer on demand: photoswitch-directed behavior of metal-porphyrin frameworks. *J. Am. Chem. Soc.* **136**, 11886–11889 (2014)
11. J.T. Joyce, F.R. Laffir, C. Silien, Layer-by-layer growth and photocurrent generation in metal-organic coordination films. *J. Phys. Chem. C* **117**, 12502–12509 (2013)
12. D.Y. Lee, D.V. Shinde, S.J. Yoon, et al., Cu-based metal-organic frameworks for photovoltaic application. *J. Phys. Chem. C* **118**, 16328–16334 (2014)
13. K. Leong, M.E. Foster, B.M. Wong, et al., Energy and charge transfer by donor-acceptor pairs confined in a metal-organic framework: a spectroscopic and computational investigation. *J. Mater. Chem. A* **2**, 3389–3398 (2014)
14. C.Y. Lee, O.K. Farha, B.J. Hong, et al., Light-harvesting metal-organic frameworks (MOFs): efficient strut-to-strut energy transfer in bodipy and porphyrin-based MOFs. *J. Am. Chem. Soc.* **133**, 15858 (2011)
15. M.C. So, S. Jin, H.J. Son, et al., Layer-by-layer fabrication of an oriented thin film based on a porphyrin-containing metal-organic framework. *J. Am. Chem. Soc.* **135**, 15698 (2013)
16. G. McDermott, S. Prince, A. Freer, et al., Crystal structure of an integral membrane light-harvesting complex from photosynthetic bacteria. *Nature* **374**, 517 (1995)
17. S. Patwardhan, S. Jin, H.J. Son, G.C. Schatz, Ultrafast energy migration in porphyrin-based metal-organic frameworks (MOFs). *MRS Online Proc. Libr.* **1539**, Mrss13-1539-d06-06 (2013)
18. C.B. Murphy, Y. Zhang, T. Troxler, et al., Probing Förster and Dexter energy-transfer mechanisms in fluorescent conjugated polymer chemosensors. *J. Phys. Chem. B* **108**, 1537 (2004)
19. J. Brey, C. Kratzer, H. Yersin, Crystal engineering as a tool for directed radiationless energy transfer in layered $\{\Lambda\text{-[Ru(bpy)}_3\text{]}\Delta\text{-[Os(bpy)}_3\text{]}\}$ (PF6)₄. *J. Am. Chem. Soc.* **122**, 2548 (2000)
20. M. Devenney, L.A. Worl, S. Gould, et al., Excited state interactions in electropolymerized thin films of RuII, OsII, and ZnII polypyridyl complexes. *J. Phys. Chem. A* **101**, 4535 (1997)
21. C.N. Fleming, P. Jang, T.J. Meyer, J.M. Papanikolas, Energy migration dynamics in a Ru (II)- and Os (II)-based antenna polymer embedded in a disordered, rigid medium. *J. Phys. Chem. B* **108**, 2205 (2004)
22. C.N. Fleming, K.A. Maxwell, J.M. DeSimone, T.J. Meyer, J.M. Papanikolas, Ultrafast excited-state energy migration dynamics in an efficient light-harvesting antenna polymer based on Ru (II) and Os (II) polypyridyl complexes. *J. Am. Chem. Soc.* **123**, 10336 (2001)
23. N. Ikeda, A. Yoshimura, M. Tsushima, T. Ohno, Hopping and annihilation of 3MLCT in the crystalline solid of [Ru (bpy)₃]²⁺X₂ (X = Cl⁻, ClO₄⁻ and PF₆⁻). *J. Phys. Chem. A* **104**, 6158 (2000)
24. C.A. Kent, D. Liu, L. Ma, J.M. Papanikolas, T.J. Meyer, W. Lin, Light harvesting in microscale metal-organic frameworks by energy migration and interfacial electron transfer quenching. *J. Am. Chem. Soc.* **133**, 12940 (2011)
25. C.A. Kent, D. Liu, T.J. Meyer, W. Lin, Amplified luminescence quenching of phosphorescent metal-organic frameworks. *J. Am. Chem. Soc.* **134**, 3991 (2012)
26. C.A. Kent, B.P. Mehl, L. Ma, et al., Energy transfer dynamics in metal-organic frameworks. *J. Am. Chem. Soc.* **132**, 12767 (2010)
27. S.A. Trammell, J. Yang, M. Sykora, et al., Molecular energy transfer across oxide surfaces. *J. Phys. Chem. B* **105**, 8895 (2001)

28. M. Tsushima, N. Ikeda, A. Yoshimura, K. Nozaki, T. Ohno, Solid-state photochemistry: energy-transfer and electron-transfer of 3CT in crystals of $[\text{Os}_x\text{Ru}_{1-x}(\text{bpy})_3]\text{X}_2$ ($x = 0-0.23$). *Coord. Chem. Rev.* **208**, 299 (2000)
29. M.D. Ward, F. Barigelletti, Control of photoinduced energy transfer between metal-polypyridyl luminophores across rigid covalent, flexible covalent, or hydrogen-bonded bridges. *Coord. Chem. Rev.* **216**, 127 (2001)
30. B. Abrahams, B. Hoskins, D. Michail, R. Robson, Assembly of porphyrin building blocks into network structures with large channels. *Nature* **369**, 727 (1994)
31. O.K. Farha, A.M. Shultz, A.A. Sarjeant, S.T. Nguyen, J.T. Hupp, Active-site-accessible, porphyrinic metal-organic framework materials. *J. Am. Chem. Soc.* **133**, 5652 (2011)
32. A.M. Shultz, A.A. Sarjeant, O.K. Farha, J.T. Hupp, S.T. Nguyen, Post-synthesis modification of a metal-organic framework to form metallosalen-containing MOF materials. *J. Am. Chem. Soc.* **133**, 13252 (2011)
33. S. Becker, A. Böhm, K. Müllen, New thermotropic dyes based on amino-substituted perylene-dicarboximides. *Chem. Eur. J.* **6**, 3984 (2000)
34. H.J. Son, S. Jin, et al., Light-harvesting and ultrafast energy migration in porphyrin-based metal-organic frameworks. *J. Am. Chem. Soc.* **135**, 862 (2013)
35. B.A. Gregg, R.A. Cormier, Doping molecular semiconductors: n-type doping of a liquid crystal perylene diimide. *J. Am. Chem. Soc.* **123**, 7959 (2001)
36. A. Breeze, A. Salomon, D. Ginley, Polymer – perylene diimide heterojunction solar cells. *Appl. Phys. Lett.* **81**, 3085 (2002)
37. H. Langhals, O. Krotz, K. Polborn, P. Mayer, A novel fluorescent dye with strong, anisotropic solid-state fluorescence, small stokes shift, and high photostability. *Angew. Chem. Int. Ed.* **44**, 2427 (2005)
38. H.J. Park, M.C. So, et al., Layer-by-layer assembled films of perylene diimide-and squaraine-containing metal-organic framework-like materials: solar energy capture and directional energy transfer. *ACS Appl. Mater. Interfaces* **8**(38), 24983–24988 (2016)
39. V. Stavila, J. Volponi, A.M. Katzenmeyer, M.C. Dixon, M.D. Allendorf, Kinetics and mechanism of metal-organic framework thin film growth: systematic investigation of HKUST-1 deposition on QCM electrodes. *Chem. Sci.* **3**(5), 1531–1540 (2012)
40. M.C. So, S. Jin, H.J. Son, G.P. Wiederrecht, O.K. Farha, J.T. Hupp, Layer-by-layer fabrication of oriented porous thin films based on porphyrin-containing metal-organic frameworks. *J. Am. Chem. Soc.* **135**(42), 15698–15701 (2013)
41. H. Lu, S. Zu, Interfacial synthesis of free-standing metal-organic framework membranes. *Eur. J. Inorg. Chem.*, **8**, 1294–1300 (2013)
42. S.D. Sathaye, K.R. Patil, D.V. Paranjape, et al., Preparation of Q-cadmium sulfide ultrathin films by a new liquid-liquid interface reaction technique (LLIRT). *Langmuir* **16**, 3487–3490 (2000)
43. C.N.R. Rao, G.U. Kulkarni, V.V. Agrawal, U.K. Gautam, M. Ghosh, U. Tumkurkar, Use of the liquid-liquid interface for generating ultrathin nanocrystalline films of metals, chalcogenides, and oxides. *J. Colloid Interface Sci.* **289**(2), 305–318 (2005)
44. C.N.R. Rao, K.P. Kalyanikutty, The liquid-liquid interface as a medium to generate nanocrystalline films of inorganic materials. *Acc. Chem. Res.* **41**(4), 489–499 (2008)
45. V.V. Agrawal, G.U. Kulkarni, C.N.R. Rao, Nature and properties of ultrathin nanocrystalline gold films formed at the organic-aqueous interface. *J. Phys. Chem.* **109**(15), 7300–7305 (2005)
46. G.L.e.a. Stansfield, Growth of nanocrystals and thin films at the water-oil interface. *Phil. Trans. R. Soc. A* **368**, 4313–4330 (2010)
47. D. Sheberla, L. Sun, M. Blood-Forsythe, et al., High electrical conductivity in Ni₃(2,3,6,7,10,11-hexaiminotriphenylene)₂ a semiconducting metal organic graphene analog. *J. Am. Chem. Soc.* **136**, 8859–8862 (2014)

48. D. Fan, P.J. Thomas, P. O'Brien, Deposition of CdS and ZnS thin films at the water/toluene interface. *J. Mater. Chem.* **17**, 1381–1386 (2007)
49. G. Wu, J. Huang, Y. Zang, et al., Porous field-effect transistor based on a semiconducting metal-organic framework. *J. Am. Chem. Soc.* **139**, 1360–1363 (2017)
50. J. Berry, T. Buonassisi, D.A. Egger, et al., Hybrid organic-inorganic perovskites (HOIPs): opportunities and challenges. *Adv. Mater.* **27**(35), 5102–5112 (2015)
51. H.S. Kim, N.G. Park, Parameters affecting I-V hysteresis of CH₃NH₃PbI₃ perovskite solar cells: effects of perovskite crystal size and mesoporous TiO₂ layer. *J. Phys. Chem. Lett.* **5**(17), 2927–2934 (2014)